

A Nonoscillatory Discontinuous Galerkin Transport Scheme on the Cubed Sphere

YIFAN ZHANG

Division of Applied Mathematics, Brown University, Providence, Rhode Island

RAMACHANDRAN D. NAIR

National Center for Atmospheric Research, Boulder, Colorado*

(Manuscript received 15 October 2011, in final form 2 February 2012)

ABSTRACT

The discontinuous Galerkin (DG) method is high order, conservative, and offers excellent parallel efficiency. However, when there are discontinuities in the solution, the DG transport scheme generates spurious oscillations that reduce the quality of the numerical solution. For applications such as the atmospheric tracer transport modeling, a nonoscillatory, positivity-preserving solution is a basic requirement. To suppress the oscillations in the DG solution, a limiter based on the Hermite-Weighted Essentially Nonoscillatory (H-WENO) method has been implemented for a third-order DG transport scheme. However, the H-WENO limiter can still produce wiggles with small amplitudes in the solutions, but this issue has been addressed by combining the limiter with a bound-preserving (BP) filter. The BP filter is local and easy to implement and can be used for making the solution strictly positivity preserving. The DG scheme combined with the limiter and filter preserves the accuracy of the numerical solution in the smooth regions while effectively eliminating overshoots and undershoots. The resulting nonoscillatory DG scheme is third-order accurate (P^2 -DG) and based on the *modal* discretization. The 2D Cartesian scheme is further extended to the cubed-sphere geometry, which employs nonorthogonal, curvilinear coordinates. The accuracy and effectiveness of the limiter and filter are demonstrated with several benchmark tests on both the Cartesian and spherical geometries.

1. Introduction

The discontinuous Galerkin (DG) method may be viewed as a hybrid approach combining the good features of two classical numerical discretization approaches, the finite-volume (FV) and finite-element methods, and exploiting the merits of both. The DG spatial discretization combined with Runge–Kutta time integration (RKDG method) provides a class of robust algorithms for solving conservation laws (Cockburn and Shu 1989; Cockburn 1997). Because of its computationally attractive features such as local and global conservation, high-order accuracy, high parallel efficiency

(petascale capability), and geometric flexibility, the DG method is becoming increasingly popular in atmospheric modeling [for the spherical geometry application, see, e.g., Giraldo et al. (2002); Nair et al. (2005a); Läuter et al. (2008)]. A recent review by Nair et al. (2011) presents various DG applications in atmospheric science with an extensive list of references.

Even though the RKDG scheme has many desirable properties, for transport equations with strong shocks or contact discontinuities, a nonlinear limiter must be employed to suppress oscillations. There are extensive studies on limiters for the low-order finite-volume methods. The slope limiters used for FV schemes can be extended to the *modal* form of DG methods (Cockburn 1997), however, this drastically reduces the high-order accuracy of the DG scheme (Iskandarani et al. 2005; Krivodonova 2007). To maintain the properties of the DG scheme, the limiter used should not reduce the order of accuracy in the region where the solution is smooth. To address this issue, Qiu and Shu (2005b) have developed high-order limiters based on the Weighted

* The National Center for Atmospheric Research is sponsored by the National Science Foundation.

Corresponding author address: R. D. Nair, Computational and Information System Laboratory, National Center for Atmospheric Research, Boulder, CO 80305.
E-mail: rnair@ucar.edu

Essentially Nonoscillatory (WENO) schemes, where the WENO-type nonoscillatory reconstruction technique serves as a limiter for the RKDG method. A major disadvantage of this type of limiter is its requirement for a wider halo region (stencil), which could potentially impede parallel efficiency. For example, a third-order DG scheme requires a 5×5 stencil (i.e., halo size of width 2 in each direction) to apply a consistent WENO limiter. Subsequently, Qiu and Shu (2005a) improved this deficiency by developing the Hermite-WENO (H-WENO) limiter, for which a more compact stencil is employed. For a third-order DG scheme, the H-WENO limiter requires only a 3×3 stencil. The DG scheme combined with an H-WENO limiter has been recently used for a system of conservation laws in several applications (Luo et al. 2007; Balsara et al. 2007). Note that a WENO or H-WENO limiter is only “essentially” nonoscillatory by design, which implies that minor wiggles may appear in the solution even after the limiter is applied to the DG scheme. Therefore, the terminology “nonoscillatory DG scheme” is used throughout the text in a weak sense.

Though the WENO-type limiters can remove spurious oscillations, there is no guarantee that they will always keep the numerical solution within the physical bounds. The numerical solution may still have small-amplitude oscillations even after the limiter is applied. In other words, these schemes are not strictly positivity preserving. For many atmospheric tracers such as humidity and mixing ratios, the global maximum and minimum values are known in advance, and such tracers have “zero tolerance” for negative values. Therefore, for tracer transport models, the positivity preservation is considered to be a basic requirement. Very recently, Zhang and Shu (2010) developed a genuinely high-order bound-preserving (BP) filter for multidimensional RKDG methods, based on the Liu and Osher (1996) one-dimensional limiter. The BP filter clips extrema of the solution that go out of the physically legitimate bounds without violating the conservation property. Two nice features of the BP filter are that it is local and that it can easily be turned into a positivity-preserving filter when the lower bound is specified as zero. Zhang and Shu (2011) further extended this maximum-principle-satisfying filter to a variety of problems including systems of equations such as the Euler and shallow-water equations. The nonoscillatory and positivity-preserving properties for the proposed DG transport scheme are achieved by applying the H-WENO limiter and BP filter, respectively.

In this paper, we first introduce the basic DG scheme, with emphasis on a P^2 modal (third order) version, and the implementation of an H-WENO limiter with a BP

filter option. The basic ideas are developed in 2D Cartesian geometry and then extended to the cubed sphere (2D curvilinear) with several benchmark tests. The remainder of the paper is organized as follows: in section 2, the modal third-order DG scheme is described and the corresponding H-WENO scheme is introduced. Section 3 describes the implementation of the nonoscillatory DG scheme on the cubed-sphere geometry. In section 4, numerical tests on both a 2D Cartesian domain and the sphere are presented to demonstrate the performance of the nonoscillatory scheme, followed by some discussion and concluding remarks in section 5.

2. Nonoscillatory DG transport scheme

We consider the two-dimensional conservative transport equation as follows:

$$\frac{\partial U}{\partial t} + \nabla \cdot \mathbf{F}(U) = S(U), \quad \text{in } \mathcal{D} \times (0, T], \quad (1)$$

where $U = U(x, y, t)$ is a conservative quantity with a given initial value of $U_0(x, y) = U(x, y, 0)$, \mathbf{F} is the flux function, $S(U)$ is a source term, and $\nabla \cdot$ is the divergence operator defined in \mathcal{D} . The DG spatial discretization procedure consists of partitioning the domain \mathcal{D} into nonoverlapping elements (cells) $I_{i,j}$, and seeking an approximate solution $U_h \approx U$ on each element. We assume the elements to be rectangular such that $I_{i,j} = [x_{i-1/2}, x_{i+1/2}] \otimes [y_{j-1/2}, y_{j+1/2}]$. The approximate solution is $U_h \in V_h^k(I_{i,j}), \forall I_{i,j} \in \mathcal{D}$, such that $U_h|_{I_{i,j}} \in P^k(I_{i,j})$, where V_h^k is the vector space of polynomials P^k up to degree k , defined over $I_{i,j}$.

A weak Galerkin formulation of the problem is obtained by multiplying (1) by a test function $\varphi_h \in V_h^k$, and integrating by parts over $I_{i,j}$, leading to

$$\begin{aligned} \int_{I_{i,j}} \frac{\partial U_h}{\partial t} \varphi_h \, dx \, dy &= \int_{I_{i,j}} \mathbf{F}(U_h) \cdot \nabla \varphi_h \, dx \, dy \\ &\quad - \oint_{\partial I_{i,j}} \varphi_h \mathbf{F}(U_h) \cdot \mathbf{n} \, ds \\ &\quad + \int_{I_{i,j}} S(U_h) \varphi_h \, dx \, dy, \quad (2) \end{aligned}$$

where $\partial I_{i,j}$ is the boundary corresponding to element $I_{i,j}$ and \mathbf{n} is the outward-facing normal vector of the boundary. The discontinuity at the element boundaries (interfaces) within \mathcal{D} is resolved by applying suitable numerical fluxes (or approximate Riemann solvers).

a. A third-order modal formulation

The integral equation (2) is the crux of the DG algorithm, the accuracy and efficiency of which are determined

by the particular choice of P^k and the quadrature rules for the integrals. An arbitrary high-order modal DG discretization on the cubed sphere is given in Nair et al. (2005b). Nevertheless, our focus here is the development of a third-order modal nonoscillatory DG scheme. Details of the “modal” and “nodal” variants of DG scheme and their relative merits can be found in Nair et al. (2011).

A major limitation of the DG scheme is the stringent Courant–Friedrichs–Lewy (CFL) stability constraint associated with explicit time stepping. For high-order DG schemes employing polynomials of degree $k > 1$, an approximate CFL limit estimate is $1/(2k + 1)$ (Cockburn 1997). This is due to the fact that the DG method has more degrees of freedom (dofs) to evolve in time per element than a typical finite-volume or finite-element method; this makes the scheme highly accurate at a higher computational cost. However, reducing the order accuracy has some benefits. It significantly improves CFL stability and allows one to implement limiting algorithms based on those designed for FV methods. A *moderate*-order DG scheme, such as a third-order one ($k = 2$), has a CFL limit (approximately 0.2) comparable to some high-order FV schemes (Chen and Xiao 2008). In certain cases, a third-order DG scheme provides a solution that is qualitatively comparable to that of a fourth-order or fifth-order WENO scheme. Therefore, in this paper our main focus is the development of a *practical* third-order DG scheme, which we will refer to as the “ P^2 -DG” scheme. For that we utilize the modal version of the DG method, which is amenable to limiting methods as used for FV schemes.

To simplify the integrals in (2), we introduce new independent variables (ξ, η) , and every element is mapped to the standard element $[-1, 1]^2$ such that

$$\xi = \frac{2(x - x_i)}{\Delta x_i}, \quad \eta = \frac{2(y - y_j)}{\Delta y_j}; \quad \xi, \eta \in [-1, 1], \quad (3)$$

where $x_i = (x_{i-1/2} + x_{i+1/2})/2$, $y_i = (y_{j-1/2} + y_{j+1/2})/2$, $\Delta x_i = x_{i+1/2} - x_{i-1/2}$, and $\Delta y_j = y_{j+1/2} - y_{j-1/2}$. The approximate solution $U_h|_{I_{i,j}} = U_{i,j}$ for an element $I_{i,j}$ can be represented in terms of modal basis functions from the set $\mathcal{B} = \{1, \xi, \eta, \xi\eta, (3\xi^2 - 1)/2, (3\eta^2 - 1)/2\}$, composed of the Legendre (orthogonal) polynomials:

$$\begin{aligned} U_h(\xi, \eta, t)|_{I_{i,j}} &= U_{i,j}^{0,0}(t) + U_{i,j}^{1,0}(t)\xi + U_{i,j}^{0,1}(t)\eta \\ &+ U_{i,j}^{1,1}(t)\xi\eta + U_{i,j}^{2,0}(t)\frac{3\xi^2 - 1}{2} \\ &+ U_{i,j}^{0,2}(t)\frac{3\eta^2 - 1}{2}, \end{aligned} \quad (4)$$

where $U_{i,j}^{l,m}(t)$, $0 \leq l + m \leq 2$, are the six dofs (or moments) associated with the P^2 -DG scheme. The moments are defined as follows:

$$U_{i,j}^{l,m}(t) = \frac{\Delta x \Delta y}{4} \int_{-1}^1 \int_{-1}^1 U_{i,j}(\xi, \eta, t) \varphi^{l,m}(\xi, \eta) d\xi d\eta, \quad (5)$$

where the test functions $\varphi^{l,m} \in \mathcal{B}$. From (5) it is clear that the first moment $U_{i,j}^{0,0}$ is the “cell average,” in an FV sense. The integrals in (2) associated with the P^2 -DG scheme are evaluated either by using the Gauss–Lobatto–Legendre (GLL) or the Gauss–Legendre (GL) grid consistent with the order of accuracy of the scheme, as shown in Fig. 1.

For the flux term in (2), we consider the local Lax–Friedrichs flux given by

$$\hat{F}(U_h^-, U_h^+) = \frac{1}{2} \{ [\mathbf{F}(U_h^+) + \mathbf{F}(U_h^-)] \cdot \mathbf{n} - \bar{\alpha}(U_h^+ - U_h^-) \},$$

where $\bar{\alpha}$ is the maximum value of the flux Jacobian (which is the local maximum wind speed for the advection problem) and U_h^-, U_h^+ denote the left (bottom) and right (top) values of the numerical solution (Cockburn 1997). This resolves the discontinuity at the element edges. Further simplification of the weak form (2) leads to the semidiscrete form, which is a system of ordinary differential equations (ODE) in time for each moment. More details of the discretization can be found in Nair et al. (2011). In short, the six modes $U_h^{l,m}$ of the DG solution on any element will follow the ODEs:

$$\frac{d}{dt} U_h^{l,m} = L(U_h^{l,m}), \quad (6)$$

where L represents DG spatial discretization resulting from (2). Thus the approximate solution U_h on each element at a new time level can be computed by solving (6) and using (4). For the present work we use the third-order Strong Stability Preserving (SSP) Runge–Kutta time integration scheme (Gottlieb et al. 2001) to solve (6).

b. The H-WENO limiter

To suppress the oscillations in the numerical solution in the presence of a shock or discontinuity, we employ the Hermite-WENO limiting strategy. The H-WENO limiting strategy for the DG scheme was first introduced by Qiu and Shu (2005a). It is a variant of the traditional WENO-type limiter (Qiu and Shu 2005b) in the sense that they share the same methodology. Once a cell is

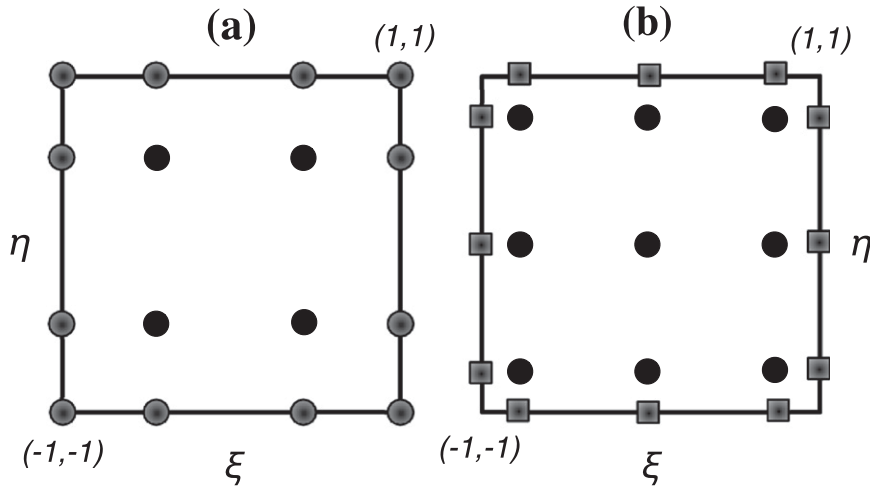


FIG. 1. For the DG discretization, every rectangular element is mapped onto a standard element $[-1, 1]^2$ with the local (ξ, η) coordinates. (a) GLL quadrature grid with 4×4 points, where on the boundary the solution points and flux points coincide. (b) GL quadrature grid with 3×3 internal points (filled circles) and three flux points on each side (filled squares). The values at the flux points are interpolated using the modal basis functions.

identified as an oscillatory (or “troubled”) cell, with a shock detection technique such as the (total variation bounded) TVB-type limiter (Cockburn et al. 1990), then all the higher-order moments are modified except for the first moment (i.e., cell average). Preservation of the cell average is required to guarantee conservation. We briefly outline the procedure below (details can be found in Shu 1997).

The first step is to reconstruct several polynomials P_n using the information from the neighboring cells, for which a family of candidate stencils are required. Each big stencil contains several small stencils (or substencils) S_n consisting of the cell $I_{i,j}$ and its neighbors, as depicted schematically in Fig. 2. The WENO scheme uses a convex combination of nonlinear weights w_n from each stencil, which depends on the local smoothness of the solution, and ultimately creates the nonoscillatory solution. The *smoothness indicators* β_n , which are a measure of the smoothness of the solution, are computed for each stencil; note that a smaller value of β_n indicates a smoother function P_n in S_n . The smoothness indicators are then used to convert precomputed linear weights (γ_n) to nonlinear weights (w_n). As a limiter, WENO modifies the high-order moments of the DG solution using a combination of nonlinear weights (Qiu and Shu 2005b).

The major difference between the H-WENO and WENO scheme is that the former uses a more compact stencil than the WENO scheme for a given order of accuracy. This makes the H-WENO algorithm more desirable for a parallel computing environment. Unlike the WENO method, which employs only the cell averages

from the neighboring cells, the H-WENO scheme relies on cell averages as well as derivative information (or “Hermite” information). For the DG discretization, derivatives are readily available, making the H-WENO limiter more computationally attractive. The H-WENO limiter retains all the nice qualities of the WENO limiter such as conservation and the nonoscillatory property, and it will not reduce the order of accuracy of the underlying scheme in the smooth region. For instance, the H-WENO stencil adopted for our P^2 -DG scheme uses a 3×3 “big” stencil, which is labeled in Fig. 2, as compared to the 5×5 stencil usually required by the WENO limiter.

To better illustrate the reconstruction process of the H-WENO limiter, we require that the reconstructed polynomial should retain the cell averages of all the cells contained in each stencil. Our focus is the implementation of the 2D H-WENO limiter for the P^2 -DG scheme. This requires a fourth-order accurate H-WENO reconstruction employing a big stencil with 3×3 cells, and a set of eight small stencils $\{S_n\}_{n=1}^8$, as shown in Fig. 2. For convenience, we denote the cells with a single index $I_\ell, \ell = \ell(i, j)$ for the reconstruction procedure. The H-WENO reconstruction involves the reconstruction of polynomials P_n in each stencil S_n , subject to some integral constraints. For example, on S_1 , we seek $P_1(x, y)$ satisfying the following constraints:

$$\int_{I_\ell} P_1(x, y) dx dy = a_0 U_\ell^{0,0}, \quad \ell = 1, 2, 4, 5$$

$$\int_{I_4} P_1(x, y) \varphi_1^{1,0} dx dy = a_1 U_4^{1,0},$$

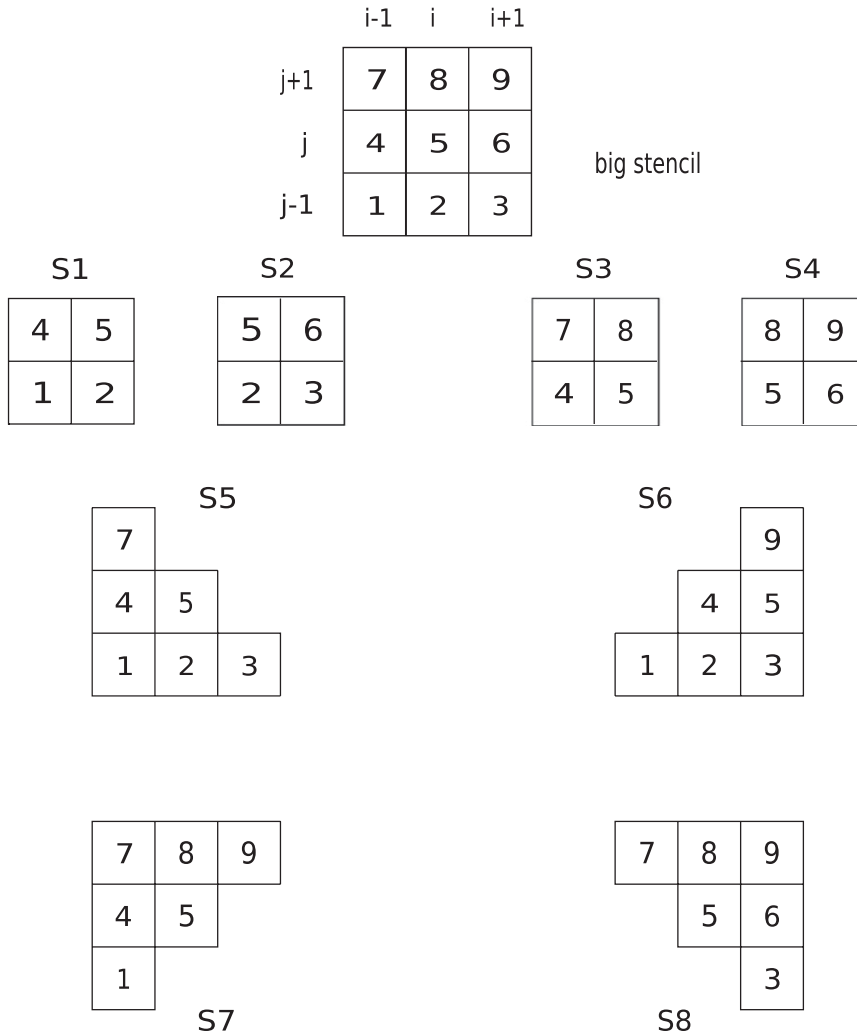


FIG. 2. The stencils used for the H-WENO reconstruction to limit a cell $I_{i,j}$ are shown for a single index $I_{\ell=5}$. For the P^2 -DG scheme, the H-WENO limiter requires a big stencil with 3×3 cells, and eight small stencils S1, S2, . . . , S8. Each small stencil contains a combination of cells from the big stencil, including the cell to be limited (I_5).

$$\int_{I_2} P_1(x,y)\phi_2^{0,1} dx dy = a_2 U_2^{0,1}, \tag{7}$$

where a_0 , a_1 , and a_2 are known coefficients. Note that the above constraints not only use the cell average ($U_{\ell}^{0,0}$) but also exploit the derivative information ($U_{\ell}^{0,1}$, $U_{\ell}^{1,0}$). Without indicating the cell dependence, a general form of $P_n(x, y)$ in terms of the local coordinates (ξ, η) can be expressed as

$$P_n(\xi, \eta) = U_n^{0,0} + U_n^{1,0}\xi + U_n^{0,1}\eta + U_n^{1,1}\xi\eta + U_n^{2,0}\frac{3\xi^2 - 1}{2} + U_n^{0,2}\frac{3\eta^2 - 1}{2}. \tag{8}$$

Using the integral constraints, (8) can be further modified for each stencil S_n . The details for the reconstruction process are given in appendix A.

As mentioned above, we use a TVB-type limiter to identify an oscillatory cell $I_{i,j}$, while keeping the cell average ($U_{ij}^{0,0}$) unchanged. Modification of higher-order moments involves several steps. First compute the optimal linear weights γ_n assigned for each reconstructed polynomial $P_n(x, y)$. The details of this may be found in Qiu and Shu (2005a); we list only the key results here. For the first-order moments $U_{ij}^{1,0}$ and $U_{ij}^{0,1}$, the linear weights are

$$\gamma_1 = \gamma_2 = \gamma_3 = \gamma_4 = \frac{11}{76}; \quad \gamma_5 = \gamma_6 = \gamma_7 = \gamma_8 = \frac{2}{19}.$$

For the second-order moments $U_{ij}^{1,1}$, $U_{ij}^{2,0}$, and $U_{ij}^{0,2}$, $\gamma_n = 1/8$, $n = 1, \dots, 8$. The smoothness indicators β_n associated with each $P_n(x, y)$ for the first-order moments $U_{ij}^{1,0}$ and $U_{ij}^{0,1}$ are, respectively,

$$\beta_n = \sum_{m=1}^2 |I_{ij}|^{m-1} \int_{I_{ij}} \left[\frac{\partial^m}{\partial x^m} P_n(x, y) \right]^2 dx dy,$$

$$\beta_n = \sum_{m=1}^2 |I_{ij}|^{m-1} \int_{I_{ij}} \left[\frac{\partial^m}{\partial y^m} P_n(x, y) \right]^2 dx dy. \quad (9)$$

And for the second-order moments $U_{ij}^{1,1}$, $U_{ij}^{2,0}$, and $U_{ij}^{0,2}$, the smoothness indicators are computed as follows:

$$\beta_n = \sum_{|m|=2}^2 |I_{ij}|^{m-1} \int_{I_{ij}} \left[\frac{\partial^{|m|}}{\partial x^{m_1} \partial y^{m_2}} P_n(x, y) \right]^2 dx dy \quad (10)$$

(see appendix B for the details of the smoothness indicator computation). The next step is to convert the linear weights γ_n into normalized nonlinear weights w_n using smooth indicators β_n :

$$w_n = \frac{\tilde{w}_n}{\sum_n \tilde{w}_n}, \quad \tilde{w}_n = \frac{\gamma_n}{(\varepsilon + \beta_n)^2},$$

where $\varepsilon = O(10^{-6})$ to prevent a zero denominator. Finally, we replace all the higher-order moments $U_{ij}^{l,m}$, $1 \leq (l + m) \leq 2$ by modified moments $\tilde{U}_{ij}^{l,m}$ using

$$\tilde{U}_{ij}^{l,m} = \sum_{n=1}^8 w_n U_n^{l,m}. \quad (11)$$

The limited approximate solution corresponding to (4) is obtained by replacing the unlimited coefficients with the limited coefficients (11), and this completes the H-WENO limiting process for the P^2 -DG scheme.

Qiu and Shu (2005a) have shown that the H-WENO limiter coupled with the DG scheme is indeed third-order accurate for smooth problems. However, just like the WENO limiter, the H-WENO limiter is also only essentially nonoscillatory, which means it may not eliminate all small oscillations near the physical bounds. This is the motivation for us to further implement a bound-preserving filter for the P^2 -DG scheme combined with the H-WENO limiter.

c. The BP filter

To preserve the initial bounds of the numerical solutions and eliminate negative densities (if positivity is

a requirement), we can apply a bound-preserving filter as an additional option. The BP filter has several attractive features. It is local, conservative, computationally cheap, and easy to implement (Zhang and Shu 2010). For P^2 -DG, the moments are evolving with respect to time. However, the gridpoint values of the approximate solution U_h on I_{ij} at any instant can be computed from the polynomial representation (4). Let $p_{ij}(x, y)$ be the modal DG polynomial on the cell I_{ij} with cell average \bar{u}_{ij} , and let S_{ij} be the local computational stencil in the gridpoint (physical) space corresponding to I_{ij} .

The BP filter essentially replaces $p_{ij}(x, y)$ with a modified polynomial $\tilde{p}_{ij}(x, y)$, such that

$$\tilde{p}_{ij}(x, y) = \hat{\theta} p_{ij}(x, y) + (1 - \hat{\theta}) \bar{u}_{ij},$$

$$\hat{\theta} = \min \left[\frac{M - \bar{u}_{ij}}{M_{ij} - \bar{u}_{ij}}, \frac{m^* - \bar{u}_{ij}}{m_{ij}^* - \bar{u}_{ij}}, 1 \right], \quad (12)$$

where the local extrema are $M_{ij} = \max_{(x,y) \in S_{ij}} p_{ij}(x, y)$ and $m_{ij}^* = \min_{(x,y) \in S_{ij}} p_{ij}(x, y)$. In (12), M and m^* are, respectively, the global maximum and minimum values of the initial condition, which are usually known in the context of a certain atmospheric tracer transport. From (12) it is clear that $\tilde{p}_{ij}(x, y)$ preserves the cell average \bar{u}_{ij} , which is a basic requirement for local conservation, for $\hat{\theta} \in [0, 1]$. More details of the filter function (12) and other applications can be found in a recent review by Zhang and Shu (2011). The positivity-preserving option is a special case of the BP filter, and can be achieved by setting $m^* = 0$. The local gridpoint stencil S_{ij} in the P^2 -DG context has a tensor product of four GLL quadrature points in each dimension or the tensor product of three GL points plus the Gauss points on the four boundaries for flux interpolation, as shown in Fig. 1.

The filter (12) is in fact based on the 1D filter developed by Liu and Osher (1996) for an FV scheme. Zhang and Shu (2010) have proved that this filter satisfies the strict maximum principle and is genuinely high order and extensible to DG applications. We note that, although the BP filter keeps the bounds of the solution in the range $[m^*, M]$, there is no guarantee that it will remove all the internal oscillations within the cells. However, the combination of the H-WENO limiter and the local BP filter addresses this issue.

3. Nonoscillatory DG scheme for cubed sphere

The cubed-sphere geometry (Sadourny 1972) has become a popular choice for the spherical grid system in global modeling because it offers a quasi-uniform rectangular grid structure on the sphere without pole

problems. This grid structure is suitable for high-order element-based Galerkin methods as well as cell-centered FV methods. There are different variants of the cubed-sphere topology, but we will consider the cubed-sphere geometry employing the equiangular central projection as described in Nair et al. (2005b). The sphere \mathcal{D} is decomposed into six identical regions by an equiangular central (gnomonic) projection of the faces of an inscribed cube. The central angles of projection $x^1 = x^1(\lambda, \theta)$, $x^2 = x^2(\lambda, \theta)$ are the local coordinates for each face such that $x^1, x^2 \in [-\pi/4, \pi/4]$, where λ and θ are the longitude and latitude of the sphere with radius R , respectively. This results in a nonorthogonal curvilinear coordinate system (x^1, x^2) , which is free of singularities; however, the edges of the six faces are discontinuous.

The metric tensor associated with the central mapping is given by

$$g_{ij} = \frac{R^2}{\rho^4 \cos^2 x^1 \cos^2 x^2} \times \begin{pmatrix} 1 + \tan^2 x^1 & -\tan x^1 \tan x^2 \\ -\tan x^1 \tan x^2 & 1 + \tan^2 x^2 \end{pmatrix},$$

where $\rho^2 = 1 + \tan^2 x^1 + \tan^2 x^2$, with tensor indices $i, j \in \{1, 2\}$. The metric term (Jacobian of the transformation) is then $\sqrt{g} = |g_{ij}|^{1/2}$. The horizontal velocity vector on the sphere $\mathbf{v}(\lambda, \theta) = (u, v)$ can be expressed in terms of covariant (u_1, u_2) and contravariant (u^1, u^2) vectors, which are related through $u_i = g_{ij} u^j$, $u^i = g^{ij} u_j$, where $g^{ij} = g_{ij}^{-1}$. For each face of the cubed sphere, covariant and contravariant vectors can be computed from (u, v) as follows:

$$\begin{bmatrix} u^1 \\ u^2 \end{bmatrix} = \mathbf{A}^{-1} \begin{bmatrix} u \\ v \end{bmatrix}, \quad \begin{bmatrix} u_1 \\ u_2 \end{bmatrix} = \mathbf{A}^T \begin{bmatrix} u \\ v \end{bmatrix},$$

$$\mathbf{A} = R \begin{bmatrix} \cos\theta(\partial\lambda/\partial x^1) & \cos\theta(\partial\lambda/\partial x^2) \\ \partial\theta/\partial x^1 & \partial\theta/\partial x^2 \end{bmatrix}, \quad (13)$$

where \mathbf{A} is local to each face of the cubed sphere such that $\mathbf{A}^T \mathbf{A} = g_{ij}$. The details of the local transformation laws and the matrix \mathbf{A} are given in Nair et al. (2005b), and will not be discussed herein.

The general (tensorial) form of the transport equation (1) in curvilinear coordinates for a scalar field ψ without a source term can be written as follows:

$$\frac{\partial\psi}{\partial t} + \frac{1}{\sqrt{g}} \frac{\partial}{\partial x^i} (u^i \sqrt{g} \psi) = 0.$$

Since the metric term \sqrt{g} is time-independent, the above equation on the cubed sphere (\mathcal{D}) can be written in the following flux form:

$$\frac{\partial}{\partial t} (\sqrt{g} \psi) + \frac{\partial}{\partial x^1} (u^1 \sqrt{g} \psi) + \frac{\partial}{\partial x^2} (u^2 \sqrt{g} \psi) = 0. \quad (14)$$

If we consider the scalar $U = \sqrt{g} \psi$, then (14) becomes the standard form as given in (1), with fluxes $\mathbf{F} = (u^1 U, u^2 U)$; moreover, (14) may be treated as a simple 2D Cartesian case in (x^1, x^2) space (Levy et al. 2007). For the DG discretization, each face of the computational domain is partitioned into nonoverlapping $N_e \times N_e$ cells (elements) such that $N_e \times N_e \times 6$ cells span the entire domain \mathcal{D} .

4. Numerical experiments

a. Cartesian tests

To validate the nonoscillatory DG scheme, we solve (1) without a source term on Cartesian domains using several benchmark tests, including a solid-body rotation test suggested by LeVeque (2002). The initial scalar fields include smooth and nonsmooth distributions to check the effectiveness of the limiter and filter. For the following tests we use the 3×3 GL quadrature grid shown in the right panel of Fig. 2, and the third-order SSP Runge–Kutta (Gottlieb et al. 2001) method for time integration.

1) ADVECTION OF A 1D IRREGULAR SIGNAL

To see the effects of the BP filter and H-WENO limiter on the P^2 -DG scheme, we first solve a simple one-dimensional form of the conservation law (1), $\psi_t + (u\psi)_x = 0$, on a periodic domain $[-\pi, \pi]$. The initial value of the scalar $\psi(x, t = 0) = \psi_0$ is given as a three-level step function (or irregular signal) in $[0, 1]$, with values of $\psi_0 = 0, 0.5, 1$ for $x \in [-\pi, \pi]$, as indicated by thin lines in Fig. 3. The computational domain consists of 80 cells with a uniform velocity of $u = 1$. In Fig. 3, the numerical solution ψ_n after one revolution (period) is shown as dashed lines. Although the BP filter keeps the numerical solution within the initial bounds $[0, 1]$ as shown in Fig. 3b, the solution remains oscillatory at the level $\psi_n = 0.5$, similar to the P^2 -DG case (Fig. 3a). However, the H-WENO limiter with the BP filter removes the oscillations (Fig. 3c) while strictly preserving the initial bounds. The P^2 -DG solution combined with the H-WENO limiter appears to be very similar to Fig. 3c (not shown), but in this case the solution is not strictly positivity preserving, as there are minor undershoots (overshoots) at $\psi_n = 0$. In other words, the purpose of the BP filter is to preserve the solution within the initial bounds; nevertheless, it has no control over the *internal* oscillations of the solution or it cannot make the solution nonoscillatory. In general, the P^2 -DG solution with the H-WENO and BP combination is essentially nonoscillatory, but preserves the bounds of the initial data.

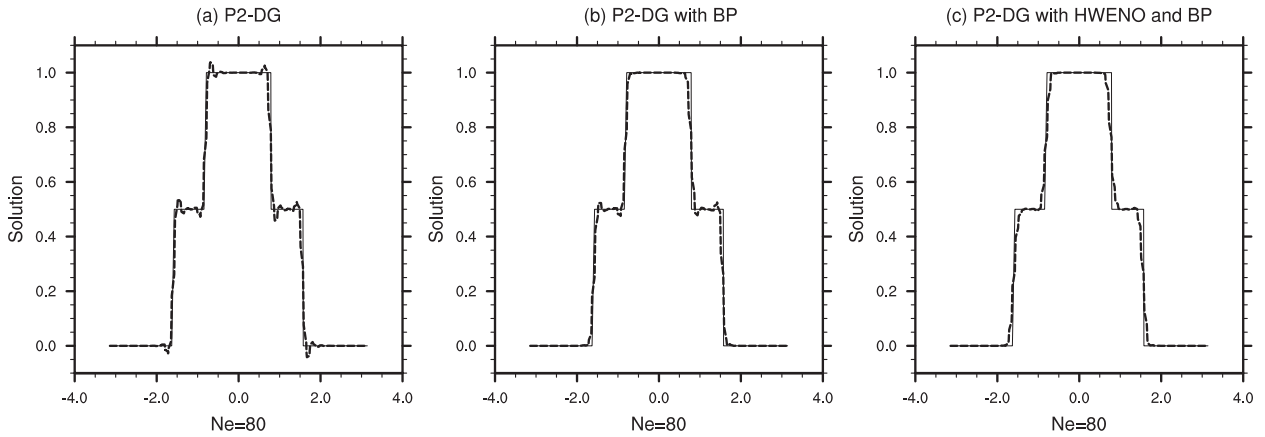


FIG. 3. Results after one complete period for the uniform advection of an irregular signal (three-level step function) on a 1D periodic domain $[-\pi, \pi]$ employing 80 cells. Reference solution is marked as thin solid lines and numerical solution is marked as dashed lines. Numerical solution with (a) P^2 -DG, (b) P^2 -DG and BP filter, and (c) P^2 -DG with both H-WENO limiter and BP filter.

2) SOLID-BODY ROTATION OF A GAUSSIAN HILL

For the 2D case we consider the conservation law $\psi_t + (u\psi)_x + (v\psi)_y = 0$ on a periodic domain \mathcal{D} . The first 2D test case is the solid-body rotation of a Gaussian hill on a square domain $\mathcal{D} = [-1, 1]^2$. The velocity field is prescribed as $(u, v) = (-\omega y, \omega x)$, where the constant angular velocity $\omega = 1$. For the solid-body rotation test, the initial scalar field translates to a circular trajectory without incurring any deformation. Moreover, the exact solution is available at any time. The initial condition is given by

$$\psi(x, y, t = 0) = a_c \exp\{-b_c[(x - x_0)^2 + (y - y_0)^2]\},$$

where a_c and b_c are taken to be 1.0 and $100/3$, respectively. For the purpose of testing the order of accuracy, we take $x_0 = 0, y_0 = 0$, and assume periodic boundary conditions. Note that for the solid-body rotation test we have used small time steps to minimize the temporal errors. An approximate estimate is given as $\Delta t = 0.5C_n\Delta$, where $C_n = 0.15$ is a CFL number less than the theoretical maximum (0.2) for P^2 -DG, and Δ is the minimum grid spacing. From Fig. 4, it is clear that both the H-WENO limiter and the BP filter are third-order accurate. Combining the filter and limiter together does not degrade the order of accuracy of the underlying DG scheme.

3) SOLID-BODY ROTATION OF A NONSMOOTH DISTRIBUTION

The second test case on the Cartesian domain is still the solid-body rotation under the same velocity field, but with a nonsmooth scalar field comprising a square block and a cone (LeVeque 2002). This field is given by

$$\psi(x, y, t = 0) = \begin{cases} 1 & \text{if } \max(|x - 0.35|, |y - 0|) \leq 0.25 \\ 1 - \hat{r} & \text{if } \hat{r} < 1 \\ 0 & \text{otherwise} \end{cases},$$

where $\hat{r} = \sqrt{(x - x_0)^2 + (y - y_0)^2}/0.35$ with $x_0 = -0.45, y_0 = 0$.

Figure 5 shows the contour plots of the numerical results and the exact solution after finishing a full circle of rotation. The grid resolution is 80×80 , which means

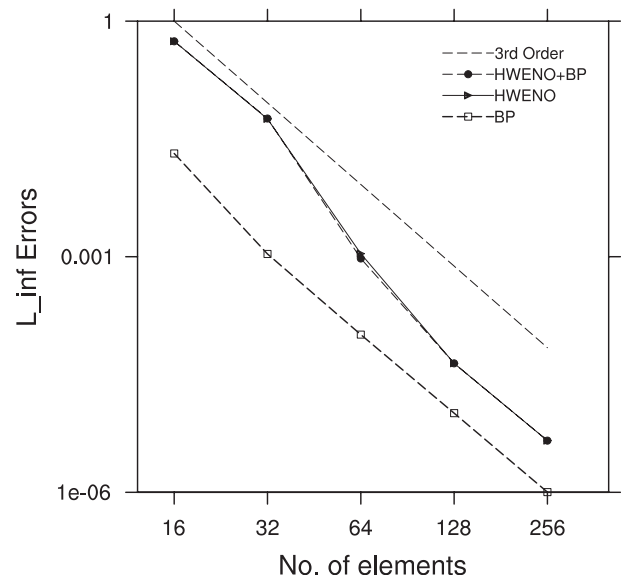


FIG. 4. Convergence plots for 2D Cartesian solid-body rotation of a Gaussian hill. The P^2 -DG transport scheme combined with the H-WENO limiter or BP filter or both is used for the convergence tests.

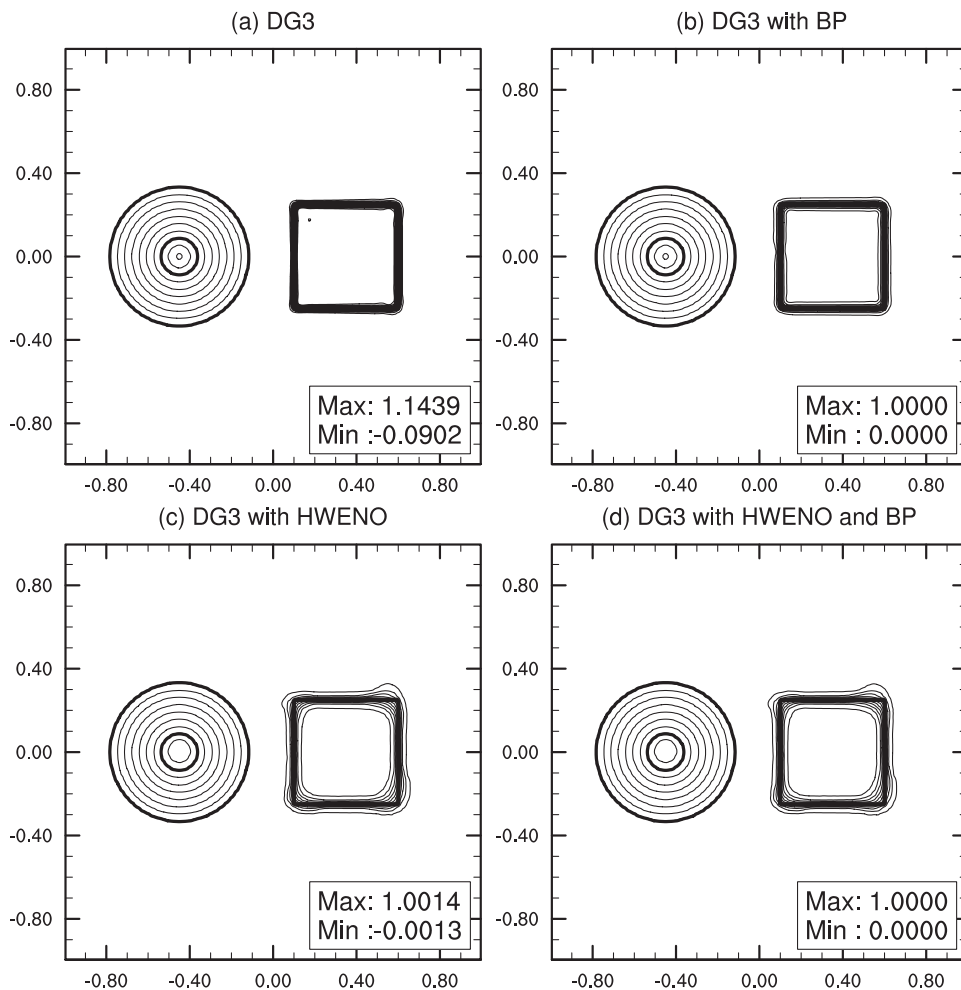


FIG. 5. Numerical results of solid-body rotation of a nonsmooth distribution (a circular cone and a square block) after one revolution with $\Delta x = \Delta y = 0.025$ using the (a) P^2 -DG scheme only, (b) P^2 -DG with the BP filter, (c) P^2 -DG with the H-WENO limiter, and (d) P^2 -DG with the H-WENO limiter and BP filter. Solid lines show contour values from 0.05 to 0.95 with increments of 0.1. Thick solid lines indicate the contour values of 0.05 and 0.75 of the exact (reference) solution.

$\Delta x = \Delta y = 0.025$, on a square domain $[-1, 1]^2$. In Fig. 6a, a 3D projection of the numerical solution is shown. It can be seen clearly from the results that the H-WENO limiter effectively removes the nonphysical oscillations that occur near the discontinuities when using a DG scheme. Figures 6a–c show a 3D projection of the solution on a 64×64 mesh with the DG scheme without the limiter or filter, with the BP filter, and with both the H-WENO limiter and BP filter, respectively. The BP filter alone helps to keep the numerical solution within the physical bounds $[0, 1]$ as shown in Fig. 6b, but there may be oscillations within these bounds. However, the H-WENO and BP combinations completely eliminate oscillations while being strictly positive definite, as evident from Fig. 6c. Thus, using the nonoscillatory DG scheme achieves a substantial improvement in the

quality of the numerical solution over using the DG scheme alone.

b. 2D spherical tests

For validating transport schemes, two types of standard tests are often used: a solid-body rotation test and a deformational flow test. We consider the solid-body rotation test suggested by Williamson et al. (1992) and Pudykiewicz (2006), and a new challenging deformational flow test described in Nair and Jablonowski (2008) and Nair and Lauritzen (2010). For the P^2 -DG scheme with a limiter (filter), we solve the transport equation (14) on the cubed sphere with the following tests. All the computations for the P^2 -DG scheme are performed using a 4×4 GLL grid as shown in Fig. 1a. Normalized standard errors l_1 , l_2 , and l_∞ and relative minimum (ψ_{\min})

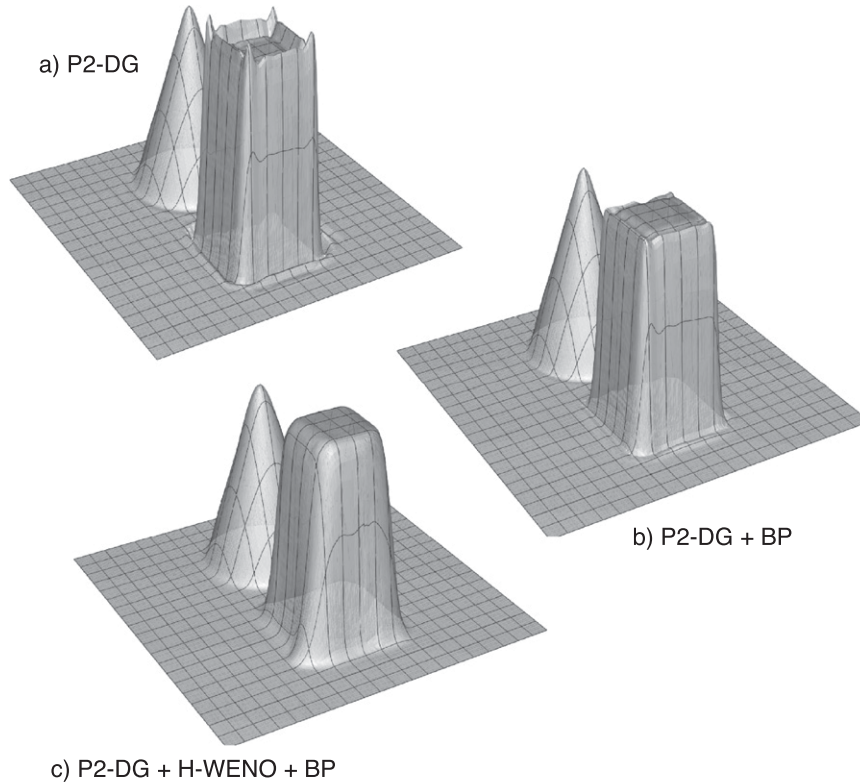


FIG. 6. A 3D perspective of the numerical solution shown in Fig. 5 but on a 64×64 grid. (a) P^2 -DG oscillatory solution, (b) P^2 -DG with the BP filter, where the bounds are preserved but oscillations are visible within the bounds $[0, 1]$, and (c) a nonoscillatory solution using the P^2 -DG scheme combined with the H-WENO limiter and the BP filter.

and maximum (ψ_{\max}) errors (Williamson et al. 1992) are used for validating the numerical scheme. The relative minimum–maximum errors are defined as

$$\psi_{\min} = \frac{\min(\psi) - \min(\psi_0)}{\Delta\psi_0}, \quad \psi_{\max} = \frac{\max(\psi) - \max(\psi_0)}{\Delta\psi_0}, \quad (15)$$

where $\Delta\psi_0 = \max(\psi_0) - \min(\psi_0)$, ψ is the numerical solution, and ψ_0 is the initial solution.

1) SOLID-BODY ROTATION: COSINE BELL

We first consider the cosine bell (CB) test (Williamson et al. 1992), which is the de facto standard test case for spherical advection problems. Since the exact solution is known at all times, error measures can be computed. The initial condition is formulated as

$$\psi(\lambda, \theta, t = 0) = \begin{cases} (h_0/2)[1 + \cos(\pi r_d/r_0)] & \text{if } r_d < r_0 \\ 0 & \text{if } r_d \geq r_0 \end{cases},$$

where $h_0 = 1000$ m is the maximum height, r_d is the great-circle distance from (λ, θ) to the center of the cosine

bell, which is initially placed at $(3\pi/2, 0)$, and $r_0 = R/3$ is the radius of the cosine bell with $R = 6.371\,22 \times 10^6$ denoting the earth’s radius. The wind field is non-divergent and defined to be

$$u = u_0(\cos\alpha \cos\theta + \sin\alpha \cos\lambda \sin\theta) \quad \text{and} \quad (16)$$

$$v = -u_0 \sin\alpha \sin\lambda, \quad (17)$$

where $u_0 = 2\pi R/12$ days, so that it takes 12 days to complete a full rotation. The orientation of the wind field can be controlled by setting the parameter α . In the following computation, α is set to be $\pi/4$, so the cosine bell goes through four vertices and all six faces. This configuration is the most challenging case for the cubed-sphere geometry. The numerical solution is computed on a $32 \times 32 \times 6$ mesh with a relatively small time step $\Delta t = 600$ s, which corresponds to an approximate CFL number of 0.02.

In Table 1, we give normalized standard error norms at $t = T = 12$ days. Normalized standard error measures are comparable to those seen in the recent high-order FV models (Chen and Xiao 2008; Ullrich et al. 2010;

TABLE 1. Normalized standard errors for ψ for the solid-body (cosine bell) rotation test after a full revolution. The third-order P^2 -DG transport scheme with different limiter (filter) combinations is used for the test. The flow orientation is along the northeast direction ($\alpha = \pi/4$) on a $32 \times 32 \times 6$ cubed-sphere mesh with a time step $\Delta t = 600$ s. Minimum and maximum heights of the cosine bell (ψ) after a revolution are indicated by Min ht and Max ht, respectively.

Scheme	l_1	l_2	l_∞	Min ht	Max ht
DG	9.75×10^{-3}	6.47×10^{-3}	5.88×10^{-3}	-5.1482	1000.9833
DG + BP	8.11×10^{-3}	5.59×10^{-3}	9.49×10^{-3}	2.65×10^{-3}	999.2054
DG + H-WENO	1.22×10^{-2}	8.44×10^{-3}	1.38×10^{-2}	-5.9211	1000.4346
DG + H-WENO + BP	9.49×10^{-3}	6.87×10^{-3}	1.32×10^{-2}	4.10×10^{-3}	996.6210

Katta et al. 2012, manuscript submitted to *Quart. J. Roy. Meteor. Soc.*). Figure 7 shows the contour plots of the numerical solution after one full rotation. From the results, it is clear that the nonoscillatory scheme will eliminate the negative values produced by the DG scheme near the foot of the bell.

2) SOLID-BODY ROTATION: MULTISCALE SIGNAL

Although the cosine-bell advection test is widely popular, it is often considered to be an easy test, especially for checking the monotonicity of the numerical scheme because the scalar distribution (cosine bell) is quasi-smooth and covers only about 10% of the entire spherical domain (elsewhere the value is set to zero). We also consider a challenging initial condition introduced in Pudykiewicz (2006), where the scalar field is a multiscale signal comprising continuous and discontinuous functions. The velocity field is the same as in the cosine-bell test (16) and (17), but the flow is oriented along the equatorial direction ($\alpha = 0$). The initial scalar field is defined as follows:

$$\psi(\lambda, \theta) = \cos^4 \theta \left\{ 2 + [f_1(\lambda) + f_2(\lambda)] \left[1 + 0.3 \sin\left(\frac{50\lambda}{9}\right) \right] \times \left[1 + 0.4 \sin\left(\frac{50\lambda}{10}\right) \right] \right\}, \quad (18)$$

where $f_1(\lambda) = -1$ for $\lambda \in D_1 \equiv [8\pi/25, 28\pi/25]$, $f_1(\lambda) = 0$ for $\lambda \in [0, 2\pi] - D_1$, $f_2(\lambda) = 1$ for $\lambda \in D_2 \equiv (28\pi/25, 39\pi/25]$, and $f_2(\lambda) = 0$ for $\lambda \in [0, 2\pi] - D_2$.

Figure 8a shows the initial condition for the multiscale signal (18), and Fig. 8b shows the numerical solution (after 12 days) with the P^2 -DG scheme and the H-WENO limiter. The experimental setup is similar to that of the solid-body rotation test, where a mesh with $32 \times 32 \times 6$ cells and a time step of $\Delta t = 600$ s are used. The P^2 -DG numerical solution without the H-WENO limiter is visually indistinguishable from that with the H-WENO limiter (Fig. 8b) and therefore not shown. Table 2 lists the normalized errors for the P^2 -DG scheme with or without the H-WENO limiter. Figures 8c,d show the value of $\psi(\lambda, \theta)$ sampled along the equator (1D data)

after one revolution using the P^2 -DG scheme without and with the H-WENO limiter, respectively. The exact solution is indicated using black dots and the numerical solution is displayed as a solid line. For this test, it is clear that the P^2 -DG scheme itself is capable of handling the shock in the multiscale signal, and the H-WENO limiter has only a marginal impact on the solution (see Fig. 8d; Table 2). Moreover, it is found that the BP filter has little or no influence on the solution, as is evident from Table 2.

3) DEFORMATIONAL FLOW ON THE SPHERE: VORTEX PROBLEM

We consider a special case of the deformational flow test, the *moving-vortex* problem, introduced in Nair and Jablonowski (2008). This test consists of two steady vortices, which are created on a sphere and whose centers are located at diametrically opposite sides. The flow field is nondivergent, time-dependent, and highly deformational. The vortices are designed to move along a great-circle trajectory while deforming, and the analytic solution is known at a given time. However, we use a *static* option for the vortices so that the vortex centers remain at the initial position and are numerically integrated for an extended period of time (60 days) as opposed to the recommended 12 days (Nair and Jablonowski 2008). The purpose of this test is to check the vortex filament formation at the smallest resolvable scale by the numerical model (Pudykiewicz 2011; Flyer and Wright 2007).

The analytic solution at time t is given as follows:

$$\psi(\lambda', \theta', t) = 1 - \tanh\left[\frac{\rho}{\gamma_0} \sin\{\lambda' - \omega(\theta')t\}\right], \quad (19)$$

where (λ', θ') are the rotated spherical coordinates with respect to the regular (λ, θ) coordinates, $\rho = \rho_0 \cos\theta'$ is the radial distance of the vortex, and the parameters $\rho_0 = 3$ and $\gamma_0 = 5$. For the current tests, the north pole of the rotated sphere is located at $(\lambda_c, \theta_c) = (3\pi/2, 0)$, which is also the center of one of the vortices. The angular velocity $\omega(\theta')$ is defined in terms of the tangential velocity V_t ,

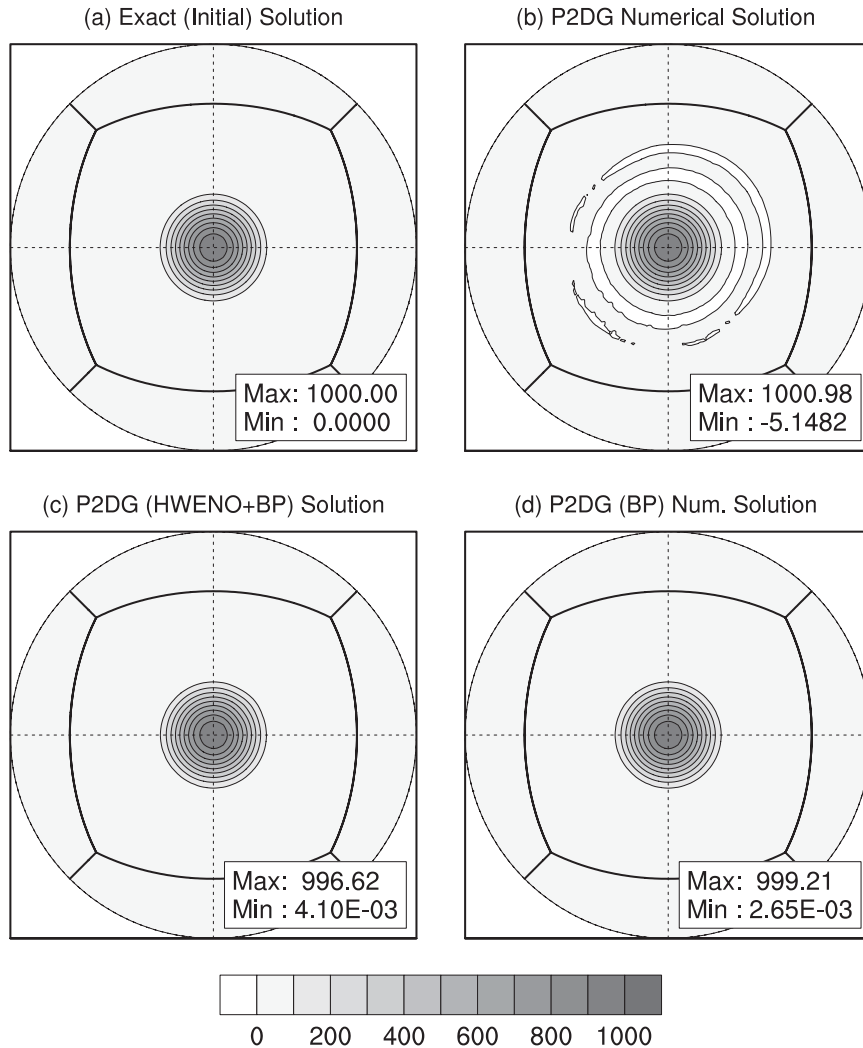


FIG. 7. An orthographic projection of the solution of the solid-body rotation of a cosine bell on the cubed sphere. The wind fields are oriented along the northeast direction ($\alpha = \pi/4$), and 12 days are required for a full revolution. (a) Initial height of the cosine bell, which ranges from 0 to 1000 units, (b) P^2 -DG solution where spurious undershoots can be seen, (c) numerical solution with the H-WENO limiter and BP filter, and (d) numerical solution with the BP filter. The cubed sphere with a mesh of $32 \times 32 \times 6$ and a time step $\Delta t = 600$ s are used for the simulation.

$$\omega(\theta') = \begin{cases} V_t/(R\rho) & \text{if } \rho \neq 0, \\ 0 & \text{if } \rho = 0, \end{cases}$$

and the tangential velocity of the vortex field is defined by

$$V_t = u_0 \frac{3\sqrt{3}}{2} \text{sech}^2(\rho) \tanh(\rho),$$

where $u_0 = 2\pi R/(12 \text{ days})$ It is scaled such that 12 model days are required for a full vortex evolution for the test recommended in Nair and Jablonowski (2008). The uniform wind field (u, v) is given by

$$u = R\omega(\theta')[\sin\theta_c \cos\theta - \cos\theta_c \cos(\lambda - \lambda_c) \sin\theta], \quad (20)$$

$$v = R\omega(\theta')[\cos\theta_c \sin(\lambda - \lambda_c)]. \quad (21)$$

The numerical experiment is performed with a relatively high-resolution mesh employing $100 \times 100 \times 6$ cells and a time step of $\Delta t = 600$ s. Figure 9 shows the solution after 36 and 60 model days. The initial condition $\psi(\lambda', \theta', t = 0)$ is shown in Fig. 9a, and the analytic (reference) solution (19) at day 60 is shown in Fig. 9d. The numerical solution with the P^2 -DG scheme and the P^2 -DG combined with the H-WENO limiter at day 36

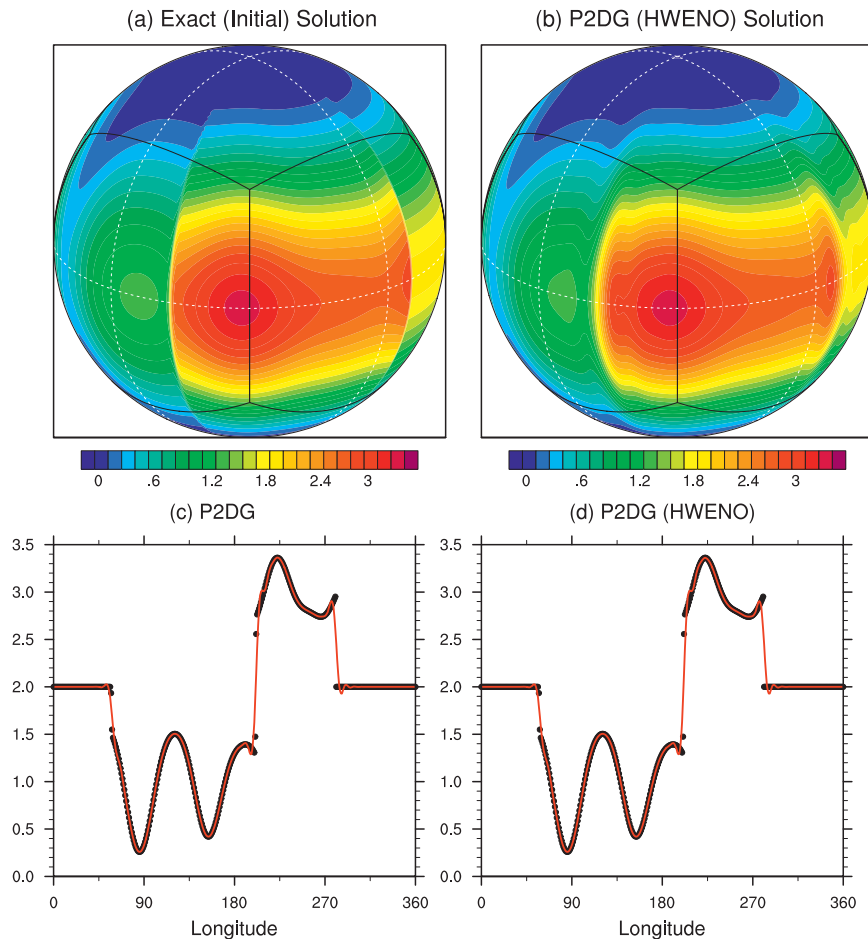


FIG. 8. Solid-body rotation test of a multiscale signal comprising continuous and discontinuous functions: (a) exact (initial) solution and (b) numerical solution after a revolution (12 days) with P^2 -DG and H-WENO; for this test, the wind field is oriented along the equator ($\alpha = 0$). The 1D numerical solution (solid lines) sampled along the equator after 12 days, and the exact reference solution marked as thick black dots: (c) P^2 -DG solution and (d) solution with P^2 -DG and H-WENO combination. The cubed-sphere mesh with $32 \times 32 \times 6$ cells and a time step $\Delta t = 1440$ s are used for the numerical simulations.

are shown in Figs. 9b,c, respectively, while the results at day 60 are shown in Figs. 9e,f, respectively. The solution with the P^2 -DG and BP filter combination is visually identical to that of the P^2 -DG scheme (Figs. 9b,e), therefore it is not shown. At this resolution the P^2 -DG scheme (with or without the BP filter) preserves the fine filaments of the vortex field and its structure appears similar to the exact solution (Fig. 9d) and comparable to

the numerical solution shown in Fig. 10 of Pudykiewicz (2011). At day 36, the solution with P^2 -DG combined with the H-WENO limiter (Fig. 9c) shows minor degradation near the narrow filament walls as compared to the P^2 -DG case (Fig. 9c). In Fig. 9f (at day 60), over the central regions of the vortex fields, some of the fine filament structures are broken or merged together as compared to the unlimited P^2 -DG case.

TABLE 2. Normalized standard errors for ψ for the solid-body rotation test with a multiscale signal on a $32 \times 32 \times 6$ cubed-sphere mesh. The third-order P^2 -DG transport scheme with H-WENO limiter and/or BP filter combinations is used for the test. The standard global error measures are based on Williamson et al. (1992).

Scheme	l_1	l_2	l_∞	ψ_{\max}	ψ_{\min}
DG	0.0088	0.0318	0.1662	6.41×10^{-4}	-1.58×10^{-6}
DG + H-WENO	0.0195	0.0335	0.1661	-1.93×10^{-4}	4.71×10^{-8}
DG + H-WENO + BP	0.0195	0.0335	0.1661	-1.93×10^{-4}	4.71×10^{-8}

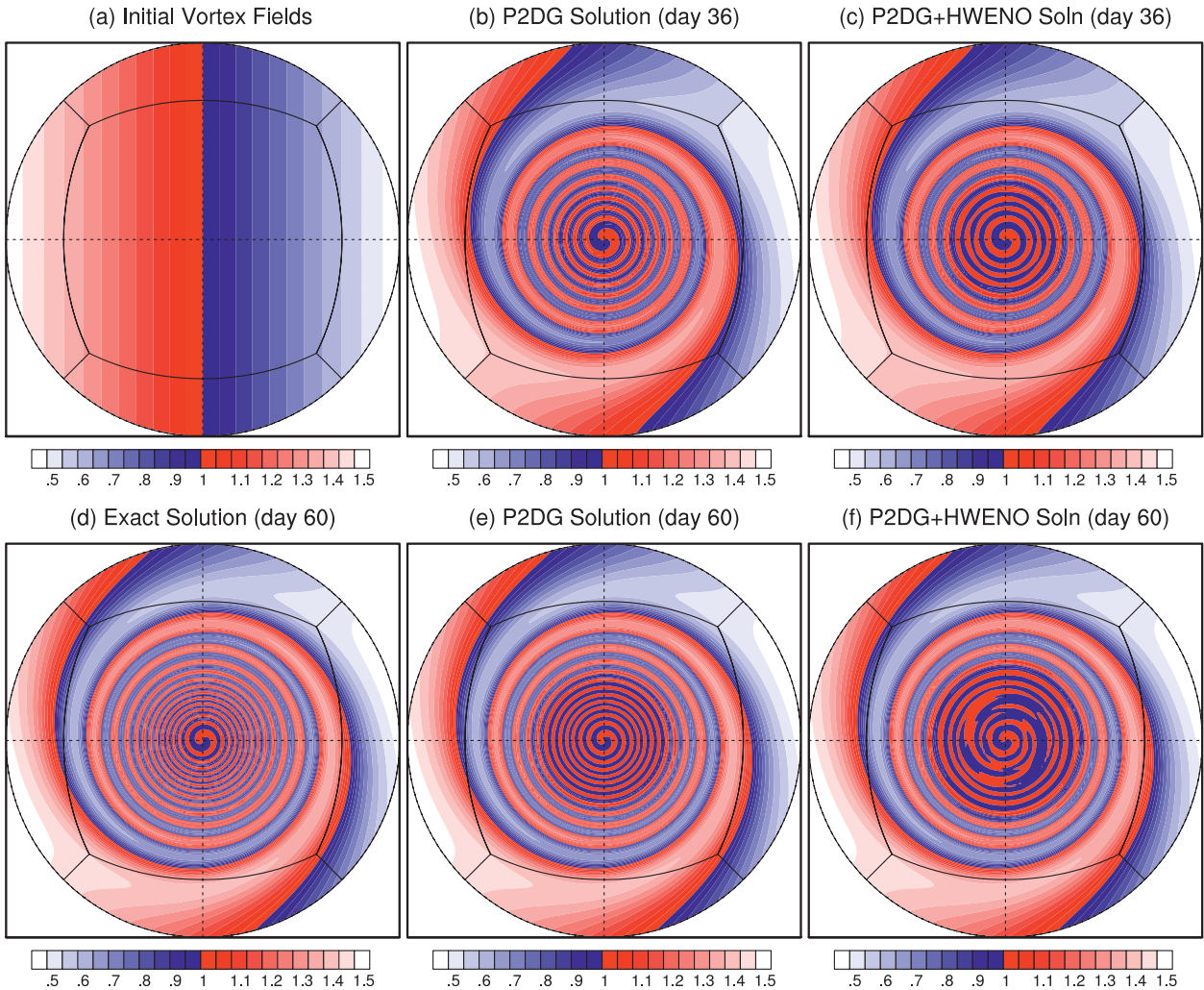


FIG. 9. The solutions for the deformational flow (vortex) test on the cubed sphere at simulated days 36 and 60: (a) initial solution; and day 36 (b) P^2 -DG solution and (c) P^2 -DG solution with H-WENO. Day 60 (d) exact (reference) solution, (e) P^2 -DG solution, and (f) P^2 -DG solution with H-WENO. Note that the numerical solutions with or without the BP filter are visually indistinguishable. The cubed-sphere mesh with $100 \times 100 \times 6$ cells and a time step $\Delta t = 600$ s are used for the numerical simulations.

Note that the deformational (vortex) test is a smooth problem for which the DG scheme does not require a limiter. This is also clear from the multiscale signal test (a quasi-smooth case) considered above. The P^2 -DG scheme is local and relies only on the cell in question, and even with the application of the BP filter, its local data dependency does not change. However, when the H-WENO limiter is applied alone with the P^2 -DG scheme, sharp gradients (thin filaments) in the solution are smoothed out because of excessive limiting. This is also due to the fact that the H-WENO limiter depends on a 3×3 wide stencil. If minor oscillations are present in a cell the limiter may be activated, employing the values from the least oscillatory cells in the stencil. This often leads to the flattening of legitimate sharp peaks, similar to the effect of a slope limiter. A way to avoid

unwanted limiting (excessive dissipation) by the H-WENO limiter is to employ better (stringent) criteria for identifying oscillatory (troubled) cells.

We have also computed the normalized standard l_1 , l_2 , and l_∞ errors after 12 model days. These values, for the P^2 -DG case with and without the BP filter, are virtually identical. When approximated to two decimal places, they are 6.93×10^{-6} , 3.30×10^{-5} , and 8.91×10^{-4} , respectively. The corresponding values for the P^2 -DG case combined with the H-WENO and BP combination are 1.31×10^{-5} , 6.81×10^{-5} , and 1.61×10^{-3} , respectively. The ψ_{\max} for all the cases is very close and approximately equal to 8.77×10^{-9} . The ψ_{\min} for the P^2 -DG case is 1.58×10^{-7} and for the other two cases it is approximately equal to 4.04×10^{-8} .

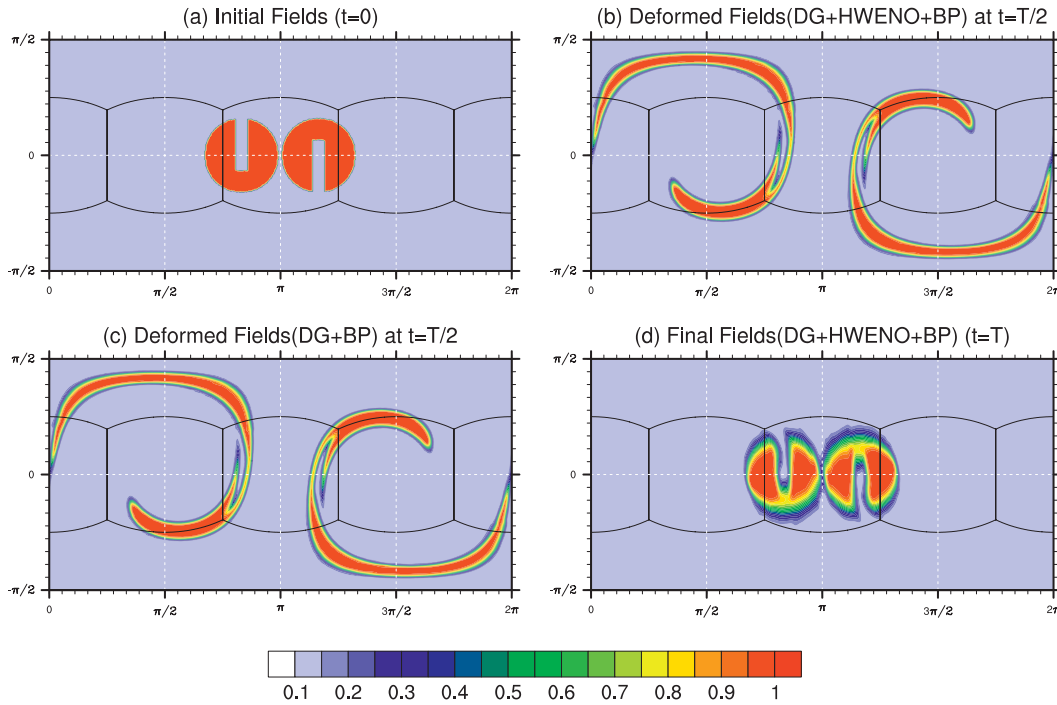


FIG. 10. Numerical solution for the deformational flow test on the cubed sphere with nonsmooth (twin slotted cylinder) initial conditions. (a) The initial slotted cylinders move along the zonal direction while deforming, and return to the initial position after making a complete revolution. The mesh size is $45 \times 45 \times 6$ and $\Delta t = 0.00125$. The P^2 -DG solution at halftime ($t = T/2$) with the (b) BP filter and H-WENO combination and (c) BP filter, respectively. (d) The slotted cylinders after one cycle of revolution (deformation) with the BP and H-WENO combination at the final time $T = 5$.

4) DEFORMATIONAL FLOW ON THE SPHERE:
SLOTTED CYLINDER

To further validate the P^2 -DG scheme on the sphere, we use a new challenging benchmark deformational flow test case proposed by Nair and Lauritzen (2010).

We are particularly interested in two cases with nonsmooth (twin slotted cylinder) and quasi-smooth (twin cosine bell) initial conditions. Note that this problem is specified in nondimensional units on a unit sphere ($R = 1$). The twin slotted cylinder is defined by

$$\psi(\lambda, \theta) = \begin{cases} c & \text{if } r_i \leq r \text{ and } |\lambda - \lambda_i| \geq r/6 \text{ for } i = 1, 2, \\ c & \text{if } r_1 \leq r \text{ and } |\lambda - \lambda_1| < r/6 \text{ and } \theta - \theta_1 < -\frac{5}{12}r, \\ c & \text{if } r_2 \leq r \text{ and } |\lambda - \lambda_2| < r/6 \text{ and } \theta - \theta_2 > \frac{5}{12}r, \\ b & \text{otherwise,} \end{cases} \quad (22)$$

where $c = 1, b = 0.1$, the radius of the cylinder $r = 1/2$, and $r_i = r_i(\lambda, \theta)$ is the great-circle distance between (λ, θ) and a specified center (λ_i, θ_i) :

$$r_i(\lambda, \theta) = \arccos[\sin\theta_i \sin\theta + \cos\theta_i \cos\theta \cos(\lambda - \lambda_i)].$$

The initial positions of the centers of the distributions are at $(\lambda_1, \theta_1) = (5\pi/6, 0)$ and $(\lambda_2, \theta_2) = (7\pi/6, 0)$, respectively. The slots are oriented in opposite directions for the two cylinders so that they are symmetric with

respect to the flow. Figure 10a shows the initial position of the slotted cylinders.

For the quasi-smooth case, the slotted cylinders are replaced by two symmetrically located cosine bells, which are defined as follows:

$$\psi(\lambda, \theta) = \begin{cases} b + ch_1(\lambda, \theta) & \text{if } r_1 < r, \\ b + ch_2(\lambda, \theta) & \text{if } r_2 < r, \\ b & \text{otherwise,} \end{cases} \quad (23)$$

TABLE 3. Normalized standard errors for ψ for the deformational flow test with the twin SC and twin CB cases on a $45 \times 45 \times 6$ mesh. The third-order P^2 -DG transport scheme with different limiter (filter) combinations is used for the test.

Scheme (tests)	l_1	l_2	l_∞	ψ_{\max}	ψ_{\min}
DG (SC)	0.1498	0.2490	0.8447	0.1748	-0.1985
DG + BP (SC)	0.1543	0.2711	0.8367	0.0000	0.0000
DG + H-WENO + BP (SC)	0.1543	0.2712	0.8361	0.0000	0.0000
DG (CB)	0.0117	0.0226	0.0301	-0.0047	-0.0261
DG + BP (CB)	0.0094	0.0206	0.0383	-0.0085	0.0000
DG + H-WENO + BP (CB)	0.0194	0.0505	0.1298	-0.0274	0.0000

where $c = 0.9$, $b = 0.1$, and

$$h_i(\lambda, \theta) = \frac{h_{\max}}{2}[1 + \cos(\pi r_i/r)] \text{ if } r_i < r, \text{ for } i = 1, 2.$$

Other parameters are the same as those used for the slotted-cylinder (SC) case.

The wind field is nondivergent but highly deformational. The initial distributions are deformed into thin filaments halfway through the simulation while they are being transported along the zonal direction by the solid-body component of the flow. Note that an exact solution for this test is only available at the final time $t = T$, and it is identical to the initial condition. The time-dependent nondivergent wind field is defined as

$$u(\lambda, \theta, t) = \kappa \sin^2(\lambda') \sin(2\theta) \cos(\pi t/T) + 2\pi \cos(\theta)/T,$$

$$v(\lambda, \theta, t) = \kappa \sin(2\lambda') \cos(\theta) \cos(\pi t/T),$$

where $\lambda' = \lambda - 2\pi t/T$, $\kappa = 2.0$, and $T = 5$ units.

Figure 10 shows the results of the deformational flow tests with the P^2 -DG scheme combined with different limiter/filter options. Figures 10c,d show the results for the slotted-cylinder case at the halftime ($t = T/2$) and final time ($t = T$). The P^2 -DG scheme combined with the H-WENO limiter and BP filter at resolution $45 \times 45 \times 6$ captures the original shape of the slotted-cylinder as shown in Fig. 10d. The P^2 -DG scheme with the BP filter produced visibly identical results (not shown). For brevity, we do not show the deformational results with the twin cosine-bell problem, but error norms are tabulated in Table 3.

As shown in Fig. 10, the nonoscillatory DG scheme preserves the discontinuity quite well and completely removes undesirable overshoots and undershoots. In Table 3, the normalized standard errors are given for different combinations of the limiter (filter) for the nonsmooth case. The l_1 , l_2 , and l_∞ errors for the nonsmooth case are significantly higher than those shown for the quasi-smooth case in Table 3. This is because the initial data for the slotted-cylinder case are severely nonsmooth (C^0 discontinuous). However, for the twin

cosine-bell case (Table 3), the results compare well with those reported in the Nair and Lauritzen (2010) paper.

We provide a rough estimate of the additional computational overhead required for the BP filter and H-WENO limiter. Both filter and limiter are applied at every stage of the third-order Runge–Kutta (RK3) time stepping scheme. As compared with the DG (oscillatory) scheme, it is found that the DG scheme and BP filter combination takes 28% more computational time, while the DG scheme combined with the H-WENO limiter and BP filter consumes about 40% more time. Note that the H-WENO scheme is selectively applied only to the cells that need limiting, while the BP filter is applied to each cell. Also, we notice that the BP filter could be applied at the last stage of the RK3 time stepping without incurring any significant change in the quality of solutions. This might be an efficient option for some application where the passive tracer transport is performed in isolation from the model dynamics.

We have also tested the effectiveness of the BP limiter in a nodal version of the DG scheme as described in Nair and Lauritzen (2010) (fourth order using 4×4 GLL points). Implementation of the BP scheme in the nodal DG version is straightforward because the solution evolves in physical (gridpoint) space. It is found that the numerical solution for the nonsmooth case is very similar to those shown in Fig. 10. However, for fifth- and higher-order nodal DG versions, the solutions are still within the physical bounds, but increasingly contaminated by internal oscillations within the elements.

5. Summary and conclusions

The discontinuous Galerkin (DG) methods are not inherently nonoscillatory. When there are discontinuities and sharp gradients in the solution, the DG transport schemes generate spurious oscillations that are unacceptable for many practical applications. The main focus of this paper is the development of a third-order DG transport scheme that is amenable to limiting processes and has more lenient CFL stability when used with explicit time stepping. A third-order modal version of the DG scheme (P^2 -DG) with 6 degrees of freedom

per element (cell) was developed in Cartesian geometry. To suppress oscillations, a limiter based on the Hermite-Weighted Essentially Nonoscillatory (H-WENO) method was applied to the P^2 -DG scheme. The H-WENO limiter uses a 3×3 computational stencil such that the oscillatory cell is located at the center. Although it suppressed oscillations, the H-WENO limiter cannot guarantee that the legitimate physical bounds of the initial solution are maintained, and oscillations of very small amplitude may still remain in the solution. To address this issue, a bound-preserving (BP) conservative filter was combined with the H-WENO limiter. The BP filter is local to the element and computationally efficient. This option provides strict positivity preservation for the P^2 -DG scheme. An explicit third-order Runge–Kutta (RK3) method was adopted for time integration.

To validate and verify the resulting nonoscillatory DG scheme, a variety of benchmark tests were performed. The H-WENO limiter and BP filter were optionally applied to remove the nonphysical oscillations and to keep the numerical solution within the physical bounds. The effects of the H-WENO limiter and BP filter on the P^2 -DG scheme were demonstrated using a simple 1D test. On the 2D Cartesian domain, two solid-body rotation tests were used. With Gaussian initial data for solid-body rotation, the test shows that the nonoscillatory scheme is indeed third order. The solid-body rotation with nonsmooth data shows that the scheme is nonoscillatory and positivity (bound) preserving. However, there is a slight degradation with the H-WENO limited solution. This could be due to “excessive limiting” on the cells that do not require limiting. A better limiting criterion, other than the TVB shock detection method currently used for the H-WENO scheme, might improve the H-WENO solution further.

The nonoscillatory P^2 -DG scheme was then extended to the spherical (cubed sphere) geometry. On the cubed sphere, a standard advection (cosine bell) test was performed first to test the nonoscillatory scheme. In addition, solid-body rotation of a multiscale signal that contained smooth and nonsmooth regions was considered. Results show that the nonoscillatory scheme eliminates all negative values and small oscillations, which occur near the foot of the cosine bell in the DG solution, without affecting the accuracy of the DG scheme. On the sphere, two deformational flow tests (with both smooth and nonsmooth fields) were used to further validate the P^2 -DG scheme with the H-WENO limiter and the BP filter. For the smoothly deforming vortex problem, the P^2 -DG scheme could easily resolve the fine filament structures of the vortex on a $100 \times 100 \times 6$ mesh after 60 model days. However, the solution

with the H-WENO limiter could not resolve the fine filaments because of excessive limiting as seen in the Cartesian case. For this test, it is found that the BP filter has only a very small impact on the fine filament structure. This indicates that the P^2 -DG scheme does not need limiting for smooth problems. If positivity preservation is an issue then the BP filter is a very good choice, and the filter does not adversely affect the quality of the DG solution.

A new challenging deformational flow test was also used to assess the performance of the nonoscillatory scheme in the presence of discontinuities. For this test, nonsmooth (slotted cylinders) and quasi-smooth (cosine bells) initial data were used. Numerical results, which were obtained on a $45 \times 45 \times 6$ mesh, show that the nonoscillatory scheme provides a good approximation to the exact solution. The standard relative errors, and the global maximum and minimum, show that there is a substantial improvement in the quality of the solution of the nonoscillatory scheme as compared to the solution obtained by the regular DG scheme. Extending the P^2 -DG transport scheme to the 3D case is straightforward at a higher computational cost. Nevertheless, a dimension-split approach might save computational expenses significantly and ease the implementation of the limiter.

Acknowledgments. The authors are thankful for Dr. Richard Loft (NCAR) and Professor Henry Tufo (CU Boulder) for the SIParCS internship support for Yifan Zhang, and Prof. C.-W. Shu (Brown University) for the inspiration. The authors gratefully acknowledge the internal review by Dr. David Hall (NCAR), and would like to thank three anonymous reviewers for their constructive comments. This project is supported by the DOE BER Program DE-SC0001658.

APPENDIX A

H-WENO Reconstructions

In section 2, we discussed the P^2 -DG discretization for each cell $I_{i,j} = I_{\ell(i,j)}$, where we considered local coordinates (ξ, η) on I_{ℓ} , and the orthogonal basis set \mathcal{B} . For the H-WENO reconstruction on each stencil S_n , $n = 1, 2, \dots, 8$, as shown in Fig. 2, the polynomials $P_n(\xi, \eta)$ given in (8) need to be modified. For the P^2 -DG scheme, a fourth-order H-WENO reconstruction is required. The reconstructed Hermite quadratic polynomials on each small stencil are derived as follows using the integral constraints associated with the smoothness indicators (9) and (10):

- On stencil S_1 , we require $P_1(x, y)$ to satisfy

$$\int_{I_\ell} P_1(x, y) dx dy = a_0 U_\ell^{0,0}, \quad \ell = 1, 2, 4, 5$$

$$\int_{I_4} P_1(x, y) \phi_4^{1,0} dx dy = a_1 U_4^{1,0}, \quad \int_{I_2} P_1(x, y) \phi_2^{0,1} dx dy = a_2 U_2^{0,1}.$$

Using the above six constraints, P_1 is reconstructed as

$$P_1(\xi, \eta) = U_5^{0,0} + (-U_4^{0,0} + U_5^{0,0} - U_4^{1,0})\xi + (-U_2^{0,0} + U_5^{0,0} - U_2^{0,1})\eta + \frac{(U_1^{0,0} - U_2^{0,0} - U_4^{0,0} + U_5^{0,0})}{4}\xi\eta$$

$$+ \frac{(-U_4^{0,0} + U_5^{0,0} - 2U_4^{1,0})}{6}\left(\frac{3\xi^2 - 1}{2}\right) + \frac{(-U_2^{0,0} + U_5^{0,0} - 2U_2^{0,1})}{6}\left(\frac{3\eta^2 - 1}{2}\right).$$

- On stencil S_2 , we require $P_2(x, y)$ to satisfy

$$\int_{I_\ell} P_2(x, y) dx dy = a_0 U_\ell^{0,0}, \quad \ell = 2, 3, 5, 6$$

$$\int_{I_6} P_2(x, y) \phi_6^{1,0} dx dy = a_1 U_6^{1,0}, \quad \int_{I_2} P_2(x, y) \phi_2^{0,1} dx dy = a_2 U_2^{0,1}$$

$$P_2(\xi, \eta) = U_5^{0,0} + (-U_5^{0,0} + U_6^{0,0} - U_6^{1,0})\xi + (-U_2^{0,0} + U_5^{0,0} - U_2^{0,1})\eta + \frac{(U_2^{0,0} - U_3^{0,0} - U_5^{0,0} + U_6^{0,0})}{4}\xi\eta$$

$$+ \frac{(U_5^{0,0} - U_6^{0,0} + 2U_6^{1,0})}{6}\left(\frac{3\xi^2 - 1}{2}\right) + \frac{(-U_2^{0,0} + U_5^{0,0} - 2U_2^{0,1})}{6}\left(\frac{3\eta^2 - 1}{2}\right).$$

- On stencil S_3 , we require $P_3(x, y)$ to satisfy

$$\int_{I_\ell} P_3(x, y) dx dy = a_0 U_\ell^{0,0}, \quad \ell = 4, 5, 7, 8$$

$$\int_{I_4} P_3(x, y) \phi_4^{1,0} dx dy = a_1 U_4^{1,0}, \quad \int_{I_8} P_3(x, y) \phi_8^{0,1} dx dy = a_2 U_8^{0,1}$$

$$P_3(\xi, \eta) = U_5^{0,0} + (-U_4^{0,0} + U_5^{0,0} - U_4^{1,0})\xi + (-U_5^{0,0} + U_8^{0,0} - U_8^{0,1})\eta + \frac{(U_4^{0,0} - U_5^{0,0} - U_7^{0,0} + U_8^{0,0})}{4}\xi\eta$$

$$+ \frac{(-U_4^{0,0} + U_5^{0,0} - 2U_4^{1,0})}{6}\left(\frac{3\xi^2 - 1}{2}\right) + \frac{(U_5^{0,0} - U_8^{0,0} + 2U_8^{0,1})}{6}\left(\frac{3\eta^2 - 1}{2}\right).$$

- On stencil S_4 , we require $P_4(x, y)$ to satisfy

$$\int_{I_\ell} P_4(x, y) dx dy = a_0 U_\ell^{0,0}, \quad \ell = 5, 6, 8, 9$$

$$\int_{I_6} P_4(x, y) \phi_6^{1,0} dx dy = a_1 U_6^{1,0}, \quad \int_{I_8} P_4(x, y) \phi_8^{0,1} dx dy = a_2 U_8^{0,1}$$

$$P_4(\xi, \eta) = U_5^{0,0} + (-U_5^{0,0} + U_6^{0,0} - U_6^{1,0})\xi + (-U_5^{0,0} + U_8^{0,0} - U_8^{0,1})\eta + \frac{(U_5^{0,0} - U_6^{0,0} - U_8^{0,0} + U_9^{0,0})}{4}\xi\eta$$

$$+ \frac{(U_5^{0,0} - U_6^{0,0} + 2U_6^{1,0})}{6}\left(\frac{3\xi^2 - 1}{2}\right) + \frac{(U_5^{0,0} - U_8^{0,0} + 2U_8^{0,1})}{6}\left(\frac{3\eta^2 - 1}{2}\right).$$

- On stencil S_5 , we require $P_5(x, y)$ to satisfy

$$\int_{I_\ell} P_5(x, y) dx dy = a_0 U_\ell^{0,0}, \quad \ell = 1, 2, 3, 4, 5, 7$$

$$\begin{aligned} P_5(\xi, \eta) = & U_5^{0,0} + \frac{(U_1^{0,0} - 2U_2^{0,0} + U_3^{0,0} - 2U_4^{0,0} + 2U_5^{0,0})}{4} \xi + \frac{(U_1^{0,0} - 2U_2^{0,0} - 2U_4^{0,0} + 2U_5^{0,0} + U_7^{0,0})}{4} \eta \\ & + \frac{(U_1^{0,0} - U_2^{0,0} - U_4^{0,0} + U_5^{0,0})}{4} \xi \eta + \frac{(U_1^{0,0} - 2U_2^{0,0} + U_3^{0,0})}{12} \left(\frac{3\xi^2 - 1}{2} \right) \\ & + \frac{(U_1^{0,0} - 2U_4^{0,0} + U_7^{0,0})}{12} \left(\frac{3\eta^2 - 1}{2} \right). \end{aligned}$$

- On stencil S_6 , we require $P_6(x, y)$ to satisfy

$$\int_{I_\ell} P_6(x, y) dx dy = a_0 U_\ell^{0,0}, \quad \ell = 1, 2, 3, 5, 6, 9$$

$$\begin{aligned} P_6(\xi, \eta) = & U_5^{0,0} + \frac{(-U_1^{0,0} + 2U_2^{0,0} - U_3^{0,0} - 2U_5^{0,0} + 2U_6^{0,0})}{4} \xi + \frac{(-2U_2^{0,0} + U_3^{0,0} + 2U_5^{0,0} - 2U_6^{0,0} + U_9^{0,0})}{4} \eta \\ & + \frac{(U_2^{0,0} - U_3^{0,0} - U_5^{0,0} + U_6^{0,0})}{4} \xi \eta + \frac{(U_1^{0,0} - 2U_2^{0,0} + U_3^{0,0})}{12} \left(\frac{3\xi^2 - 1}{2} \right) \\ & + \frac{(U_3^{0,0} - 2U_6^{0,0} + U_9^{0,0})}{12} \left(\frac{3\eta^2 - 1}{2} \right). \end{aligned}$$

- On stencil S_7 , we require $P_7(x, y)$ to satisfy

$$\int_{I_\ell} P_7(x, y) dx dy = a_0 U_\ell^{0,0}, \quad \ell = 1, 4, 5, 7, 8, 9$$

$$\begin{aligned} P_7(\xi, \eta) = & U_5^{0,0} + \frac{(-2U_4^{0,0} + 2U_5^{0,0} + U_7^{0,0} - 2U_8^{0,0} + U_9^{0,0})}{4} \xi + \frac{(-U_1^{0,0} + 2U_4^{0,0} - 2U_5^{0,0} - U_7^{0,0} + 2U_8^{0,0})}{4} \eta \\ & + \frac{(U_4^{0,0} - U_5^{0,0} - U_7^{0,0} + U_8^{0,0})}{4} \xi \eta + \frac{(U_7^{0,0} - 2U_8^{0,0} + U_9^{0,0})}{12} \left(\frac{3\xi^2 - 1}{2} \right) \\ & + \frac{(U_1^{0,0} - 2U_4^{0,0} + U_7^{0,0})}{12} \left(\frac{3\eta^2 - 1}{2} \right). \end{aligned}$$

- On stencil S_8 , we require $P_8(x, y)$ to satisfy

$$\int_{I_\ell} P_8(x, y) dx dy = a_0 U_\ell^{0,0}, \quad \ell = 3, 5, 6, 7, 8, 9$$

$$\begin{aligned} P_8(x, y) = & U_5^{0,0} + \frac{(-2U_5^{0,0} + 2U_6^{0,0} - U_7^{0,0} + 2U_8^{0,0} - U_9^{0,0})}{4} \xi + \frac{(-U_3^{0,0} - 2U_5^{0,0} + 2U_6^{0,0} + 2U_8^{0,0} - U_9^{0,0})}{4} \eta \\ & + \frac{(U_5^{0,0} - U_6^{0,0} - U_8^{0,0} + U_9^{0,0})}{4} \xi \eta + \frac{(U_7^{0,0} - 2U_8^{0,0} + U_9^{0,0})}{12} \left(\frac{3\xi^2 - 1}{2} \right) \\ & + \frac{(U_3^{0,0} - 2U_6^{0,0} + U_9^{0,0})}{12} \left(\frac{3\eta^2 - 1}{2} \right). \end{aligned}$$

APPENDIX B

The Smoothness Indicator

Here we give the explicit formulation of the smoothness indicators (β_n) in (9) and (10) associated with all the higher-order moments of the P^2 -DG for each reconstructed polynomial $P_n(x, y)$. For notational convenience, we assume $P_n(x, y)$ is expressed in the general form

$$P_n(\xi, \eta) = U_n^{0,0} + U_n^{1,0}\xi + U_n^{0,1}\eta + U_n^{1,1}\xi\eta + U_n^{2,0}\frac{3\xi^2 - 1}{2} + U_n^{0,2}\frac{3\eta^2 - 1}{2}.$$

Combined with the coefficients given in appendix A, one can compute the smoothness indicators from the formulas listed below.

- For the mode $U_{ij}^{1,0}$, we require

$$\beta_n = \sum_{m=1}^2 |I_{ij}|^{m-1} = \int_{I_{ij}} \left[\frac{\partial^m}{\partial x^m} P_n(x, y) \right]^2 dx dy.$$

For each $P_n(x, y)$, this gives

$$\beta_n = 4(U_n^{1,0})^2 + \frac{4}{3}(U_n^{1,1})^2 + 156(U_n^{2,0})^2.$$

- For the mode $U_{ij}^{0,1}$, we require

$$\beta_n = \sum_{m=1}^2 |I_{ij}|^{m-1} \int_{I_{ij}} \left[\frac{\partial^m}{\partial y^m} P_n(x, y) \right]^2 dx dy.$$

For each $P_n(x, y)$,

$$\beta_n = 4(U_n^{0,1})^2 + \frac{4}{3}(U_n^{1,1})^2 + 156(U_n^{0,2})^2.$$

- For the higher-order modes, $U_{ij}^{1,1}, U_{ij}^{2,0}, U_{ij}^{0,2}$, we require

$$\beta_n = \sum_{|m|=2}^2 |I_{ij}|^{m-1} \int_{I_{ij}} \left[\frac{\partial^{|m|}}{\partial x^{m_1} \partial y^{m_2}} P_n(x, y) \right]^2 dx dy.$$

For each $P_n(x, y)$,

$$\beta_n = 16[(U_n^{1,1})^2 + 9(U_n^{2,0})^2 + 9(U_n^{0,2})^2].$$

REFERENCES

Balsara, D. S., C. Altman, C.-D. Munz, and M. Dumbser, 2007: Sub-cell based indicator for troubled zones in RKDG schemes and a novel class of hybrid RKDG+HWENO schemes. *J. Comput. Phys.*, **226**, 586–620.

Chen, C., and F. Xiao, 2008: Shallow water model on cubed-sphere by multi-moment finite volume method. *J. Comput. Phys.*, **227**, 5019–5044.

Cockburn, B., 1997: An introduction to the Discontinuous-Galerkin method for convection-dominated problems. *Advanced Numerical Approximation of Nonlinear Hyperbolic Equations*, A. Quarteroni, Ed., Vol. 1697, *Lecture Notes in Mathematics*, Springer, 151–268.

—, and C.-W. Shu, 1989: TVB Runge-Kutta local projection discontinuous Galerkin finite element method for conservation laws II: General framework. *Math. Comput.*, **52**, 411–435.

—, S. Hou, and C.-W. Shu, 1990: TVB Runge-Kutta local projection discontinuous Galerkin finite element method for conservation laws IV: The multidimensional case. *Math. Comput.*, **54**, 545–581.

Flyer, N., and G. B. Wright, 2007: Transport schemes on a sphere using radial basis functions. *J. Comput. Phys.*, **226**, 1059–1084.

Giraldo, F., J. Hesthaven, and T. Warburton, 2002: Nodal high-order discontinuous Galerkin methods for spherical shallow water equations. *J. Comput. Phys.*, **181**, 499–525.

Gottlieb, S., C.-W. Shu, and E. Tadmor, 2001: Strong stability-preserving high-order time discretization methods. *SIAM Rev.*, **43** (1), 89–112.

Iskandarani, M., J. Levin, B.-J. Choi, and D. Haidgovel, 2005: Comparison of advection schemes for high-order h-p finite element and finite volume methods. *Ocean Modell.*, **10**, 233–252.

Krivodonova, L., 2007: Limiters for high-order discontinuous Galerkin methods. *J. Comput. Phys.*, **226**, 879–896.

Läuter, M., F. X. Giraldo, D. Handorf, and K. Dethloff, 2008: A discontinuous Galerkin method for shallow water equations in spherical triangular coordinates. *J. Comput. Phys.*, **227**, 10 226–10 242.

LeVeque, R. J., 2002: *Finite Volume Methods for Hyperbolic Problems*. Cambridge University Press, 558 pp.

Levy, M. N., R. D. Nair, and H. M. Tufo, 2007: High-order Galerkin method for scalable global atmospheric models. *Comput. Geosci.*, **33**, 1022–1035.

Liu, X.-D., and S. Osher, 1996: Nonoscillatory high order accurate self-similar maximum principle satisfying shock capturing schemes I. *SIAM J. Numer. Anal.*, **33**, 760–779.

Luo, H., J. D. Baum, and R. Lohner, 2007: A Hermite WENO-based limiter for discontinuous Galerkin method on unstructured grids. *J. Comput. Phys.*, **225**, 686–713.

Nair, R. D., and C. Jablonowski, 2008: Moving vortices on the sphere: A test case for horizontal advection problems. *Mon. Wea. Rev.*, **136**, 699–711.

—, and P. H. Lauritzen, 2010: A class of deformational flow test cases for linear transport problems on the sphere. *J. Comput. Phys.*, **229**, 8868–8887.

—, S. Thomas, and R. Loft, 2005a: A discontinuous Galerkin global shallow water model. *Mon. Wea. Rev.*, **133**, 876–888.

—, —, and —, 2005b: A discontinuous Galerkin transport scheme on the cubed sphere. *Mon. Wea. Rev.*, **133**, 814–828.

—, M. N. Levy, and P. H. Lauritzen, 2011: Emerging numerical methods for atmospheric modeling. *Numerical Techniques for Global Atmospheric Models*, P. Lauritzen et al., Eds., Vol. 80, *Lecture Notes in Computational Science and Engineering*, Springer, 251–311.

Pudykiewicz, J. A., 2006: Numerical solution of the reaction-advection-diffusion equation on the sphere. *J. Comput. Phys.*, **213**, 358–390.

- , 2011: On numerical solution of the shallow water equations with chemical reactions on icosahedral geodesic grid. *J. Comput. Phys.*, **230**, 1956–1991.
- Qiu, J., and C.-W. Shu, 2005a: Hermite WENO schemes and their application as limiters for Runge–Kutta discontinuous Galerkin method II: Two dimensional case. *Comput. Fluids*, **34**, 642–663.
- , and —, 2005b: Runge–Kutta discontinuous Galerkin method using WENO limiters. *SIAM J. Sci. Comput.*, **26**, 907–929.
- Sadourny, R., 1972: Conservative finite-difference approximations of the primitive equations on quasi-uniform spherical grids. *Mon. Wea. Rev.*, **100**, 136–144.
- Shu, C.-W., 1997: Essentially non-oscillatory and weighted essentially non-oscillatory schemes for hyperbolic conservation laws. *Advanced Numerical Approximation of Nonlinear Hyperbolic Equations*, A. Quarteroni, Ed., Vol. 1697, *Lecture Notes in Mathematics*, Springer, 325–432.
- Ullrich, P. A., C. Jablonowski, and B. van Leer, 2010: High-order finite-volume methods for the shallow-water equations on the sphere. *J. Comput. Phys.*, **229**, 6104–6134.
- Williamson, D. L., J. B. Drake, J. J. Hack, R. Jakob, and P. N. Swarztrauber, 1992: A standard test set for numerical approximations to the shallow water equations in spherical geometry. *J. Comput. Phys.*, **102**, 211–224.
- Zhang, X., and C.-W. Shu, 2010: On maximum-principle-satisfying high order schemes for scalar conservation laws. *J. Comput. Phys.*, **229**, 3091–3120.
- , and —, 2011: Maximum-principle-satisfying and positivity-preserving high-order schemes for conservation laws: Survey and new developments. *Proc. Roy. Soc.*, **A467**, 2752–2776.